https://doi.org/10.5194/egusphere-2026-3286
Preprint. Discussion started: 1 July 2026

Vertical Structure and Seasonal Evolution of Atmospheric Oxidizing Capacity across Urban and Rural Regions: Observational Constraints from OH Radical Production Pathways

Tiliang Zou[a, ★], Chengzhi Xing[b, ★,*], Zhijian Tang[c], Yikai Li[a], Zhenyi Chen[d],
Xiao Liang[e], Wei Tan[b], Cheng Liu[c,f,g,*]

[a] School of Environmental Science and Optoelectronic Technology, University of Science and Technology of China, Hefei 230026, China
[b] Key Lab of Environmental Optics & Technology, Anhui Institute of Optics and Fine Mechanics, Hefei Institutes of Physical Science, Chinese Academy of Sciences, Hefei, 230031, China
[c] Department of Precision Machinery and Precision Instrumentation, University of Science and Technology of China, Hefei 230026, China
[d] State Environmental Protection Key Laboratory of Food Chain Pollution Control, Beijing Technology and Business University, Beijing, 100048, China
[e] China National Environmental Monitoring Centre, Beijing, 100012, China
[f] Anhui Institute of Optics and Fine Mechanics, Hefei Institutes of Physical Science, Chinese Academy of Sciences, Hefei 230031, China
[g] Key Laboratory of Precision Scientific Instrumentation of Anhui Higher Education Institutes, University of Science and Technology of China, Hefei 230026, China

★ These authors contributed equally to this work.

**Corresponding to*: Chengzhi Xing (xingcz@aiofm.ac.cn); Cheng Liu (chliu81@ustc.edu.cn)

Abstract

Atmospheric oxidizing capacity (AOC) drives the formation of secondary pollutants, yet conventional surface observations fail to resolve its pronounced vertical heterogeneity, often leading to incomplete interpretations of regional pollution chemistry. Using ground-based hyperspectral vertical remote sensing observations collected between March and August 2023 at representative urban (AHU) and rural (CF) sites in the Yangtze-Huai River Basin, we quantified the vertical contributions of HONO, HCHO, and O_3 photolysis to OH production. AOC showed a strong positive correlation with aerosol loading (R = 0.88–0.93), indicating that enhanced atmospheric oxidation promotes secondary aerosol formation. In urban air masses, the AOC regime exhibited distinct vertical stratification. Rapid oxidation below 1 km was primarily driven by HCHO and HONO, whereas O_3 photolysis became the dominant OH source above 2.8 km, accounting for more than 74% of total OH production. Urban OH production transitioned from near surface HONO dominance in spring ($P(OH)_{HONO}=4.43\times10^{-4}$ ppb·s^{-1}) to HCHO dominance in summer ($P(OH)_{HCHO}=5.22\times10^{-4}$ ppb·s^{-1}). A pronounced elevated HONO enhancement layer emerged near 2.4 km during summer, driven by intensified heterogeneous conversion, with a peak contribution of 30.6% and a conversion rate $C_{(HONO)}$ of 0.053 h^{-1}. By contrast, near surface OH production at the rural site remained consistently dominated by biogenic HCHO in both spring and summer ($P(OH)_{HCHO}=1.82\times10^{-3}$ ppb·s^{-1}). These findings challenge the conventional assumption that heterogeneous chemistry is confined to the near surface atmosphere. They further provide critical vertical constraints for three-dimensional atmospheric chemistry models and offer a mechanistic explanation for the limited effectiveness of surface-based NOx mitigation strategies under vertically decoupled upper-atmospheric photochemistry.

Keywords: Atmospheric oxidizing capacity, Vertical profiles, Hydroxyl radical, Urban-rural contrast, Seasonal evolution

1. Introduction

AOC governs the transformation, lifetime, and environmental impacts of atmospheric pollutants and plays a central role in regional air-quality evolution and climate feedbacks(Dai et al., 2023; Fiore et al., 2024; Lelieveld et al., 2019; Monks et al., 2009). Hydroxyl radicals (OH), the primary atmospheric oxidant, drive the oxidation of volatile organic compounds (VOCs), nitrogen oxides (NOx), and other reduced trace gases, thereby regulating the formation of ozone (O_3) and secondary organic aerosols (SOA)(Li et al., 2025b; Mao et al., 2010; Price et al., 2025; Wolfe et al., 2019; Xing et al., 2025; Zong et al., 2018). In heavily polluted regions such as the Yangtze-Huai River Basin, the coexistence of anthropogenic and biogenic emissions introduces strong nonlinearity into precursor distributions and photochemical processes, resulting in pronounced spatial and temporal variability in atmospheric oxidation(Dai et al., 2023; Li et al., 2021a; Lu et al., 2013; Sahu et al., 2021; Tan et al., 2019). Most previous studies have characterized regional photochemistry using surface observations. However, growing evidence indicates that AOC exhibits substantial vertical heterogeneity within the boundary layer, with major implications for pollutant formation, accumulation, and transport(Liao et al., 2024; Pan et al., 2024; Shen et al., 2025; Vo et al., 2018). Resolving the vertical structure of AOC is therefore essential for understanding regional atmospheric chemistry.

Daytime OH production primarily originates from the photolysis of O_3, nitrous acid (HONO), and VOC oxidation intermediates represented by formaldehyde

https://doi.org/10.5194/egusphere-2026-3286
Preprint. Discussion started: 1 July 2026

(HCHO) (Dai et al., 2023; Nan et al., 2017; Ran et al., 2024; Yang et al., 2022). Together, these pathways account for more than 80% of total OH production and constitute the dominant photochemical oxidation framework(Dai et al., 2023; Nan et al., 2017; Yang et al., 2022). HONO photolysis is particularly important under strong near surface photochemical conditions associated with traffic emissions(Li et al., 2021b; Ye et al., 2023). HCHO, a key intermediate of VOC oxidation, sustains OH recycling in photochemically active and VOC-sensitive environments(Liu et al., 2023; Wu et al., 2023). By contrast, the contribution from O_3 photolysis increases with altitude as NO titration weakens, allowing $O(^1D)$ mediated OH production to become increasingly important above ~1 km(Liu et al., 2022b; Monks et al., 2015).

Contrasting precursor emissions between urban and rural environments fundamentally alter the vertical pathways of OH production. In urban areas, dense traffic and industrial emissions maintain extremely high near surface NOx concentrations, while heterogeneous conversion of NO_2 accounts for approximately 70–80% of HONO formation(Li et al., 2025a, 2021c). Strong NO titration simultaneously suppresses O_3, producing steep vertical chemical gradients controlled by local emissions and rapid photochemistry. Rural regions, in contrast, are more strongly influenced by biogenic VOC emissions and regional transport. Elevated HCHO and O_3 concentrations therefore exhibit comparatively homogeneous vertical distributions shaped by large-scale mixing and transport processes(Lu et al., 2019; Ren et al., 2022; Xing et al., 2017; Xue et al., 2022). These contrasts imply that the dominant OH production pathway may shift fundamentally with altitude, transitioning from near surface HONO photolysis to HCHO or O_3 driven oxidation in the middle and upper boundary layer(Dai et al., 2023; Xing et al., 2024b; Yang et al., 2022). Yet direct observational evidence for such vertical transitions remains scarce, as most previous studies relied primarily on surface measurements and could not resolve the associated vertical heterogeneity(He et al., 2023; Zhang et al., 2020). This limitation not only introduces substantial uncertainty into regional OH budgets, but also constrains the ability of chemical transport models to accurately represent atmospheric oxidation. More critically, it may bias pollution control strategies. Ignoring persistent oxidation aloft could substantially reduce the effectiveness of surface-based NOx mitigation policies, leading to large uncertainties in regional air-quality management.

To address these gaps, this study targets typical urban and rural areas in the Yangtze-Huai River Basin to reveal the vertical evolution of OH radical generation pathways across seasons. Our objectives are to elucidate: (1) The vertical mechanism shift in urban-rural AOC from near surface emission driven to mid-to-upper tropospheric photochemistry dominated during spring and summer; (2) How this vertical transition is spatially decoupled due to differences in urban-rural emission structures. These results will provide direct observational evidence for developing a vertical AOC assessment framework and offer critical scientific support for regional air quality modeling and collaborative emission reduction strategies.

2. Method and methodology

2.1 Vertical measurements

This study was conducted at two representative urban-rural sites in the Yangtze-Huai River Basin: Anhui University (AHU, 31.78°N, 117.20°E, a commercial and traffic intensive area) and Changfeng (CF, 32.21°N, 117.18°E, a farm and agricultural area) (Figure 1). The sites are separated by ~49.2 km, ensuring strong urban-rural contrast. From March to August 2023, identical ground-based hyperspectral vertical

https://doi.org/10.5194/egusphere-2026-3286
Preprint. Discussion started: 1 July 2026

remote sensing instruments were deployed at both sites to measure vertical profiles of HONO, HCHO, and O_3. The AHU instrument was mounted on a 25 m rooftop (azimuth angle 353°), while the CF instrument was installed on a 2 m container top (azimuth angle 209°). The instrument comprises three core components: a telescope, a spectrometer (spectral range: UV: 296–408 nm, VIS: 420–565 nm), and a control and data acquisition module, as detailed in our previous work(Liu et al., 2022a; Xing et al., 2024a, c; Zou et al., 2025). The measurements were performed using a complete elevation angle sequence of 1°, 2°, 3°, 4°, 5°, 6°, 8°, 10°, 15°, 30°, and 90°. A full scanning cycle required approximately 12 min, which defined the temporal resolution of the retrieved vertical profiles.

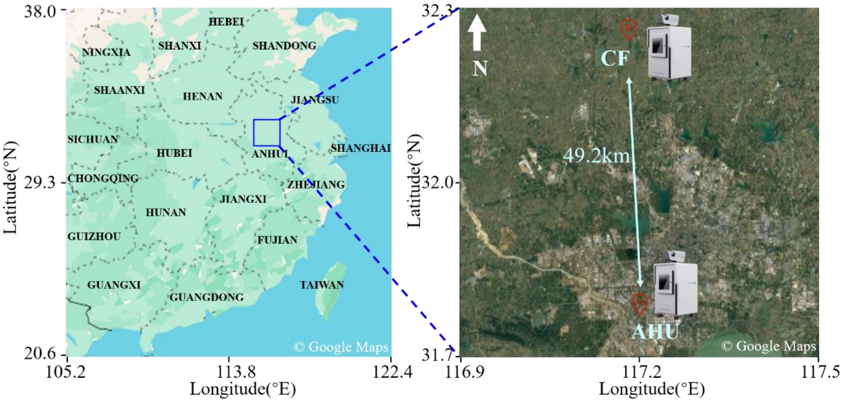

Figure 1. Schematic diagram of instrument site locations.

2.2 Data analysis

Differential slant column densities (DSCDs) of O_4, HONO, HCHO, and O_3 were retrieved using the differential absorption principle and least squares algorithm. The retrieval settings for O_4, HCHO, and O_3 adopted the parameters recommended by the CINDI-2 intercomparison campaign(Kreher et al., 2020), while those for HONO were based on Wang et al.(Wang et al., 2020) and Xing et al.(Xing et al., 2024a). To account for the ring effect arising from Rayleigh scattering, Raman scattering, and solar Fraunhofer lines, a Ring spectrum calculated by DOASIS was incorporated into the fitting process. Detailed parameter settings for O_4, HONO, HCHO, and O_3 are listed in Table S1. Prior to data analysis, dark current and offset were subtracted from all measured spectra. To mitigate the strong influence of stratospheric absorption, only spectra measured at solar zenith angles (SZA) < 75° were used(Song et al., 2023a; Xing et al., 2023). For data quality control, all retrieval results were strictly filtered to retain only data with a root mean square (RMS) of spectral fit $\leq 1\times10^{-3}$, ensuring retrieval reliability and stability. Figure S1 displays spectral fit examples for O_4, HONO, HCHO, and O_3.

Vertical profiles of aerosols and trace gases (HONO, HCHO, O_3) were retrieved using the optimal estimation method (OEM) with the pseudo-spherical vector linear discrete ordinate radiative transfer model (VLIDORT) as the forward model(Spurr, 2006). The retrieval process estimates the posterior state vector x by minimizing the cost function χ^2:

$$\chi^2 = (\boldsymbol{y} - \boldsymbol{F}(\boldsymbol{x},\boldsymbol{b}))^T \boldsymbol{S}_\varepsilon^{-1} (\boldsymbol{y} - \boldsymbol{F}(\boldsymbol{x},\boldsymbol{b})) + (\boldsymbol{x} - \boldsymbol{x}_a)^T \boldsymbol{S}_a^{-1} (\boldsymbol{x} - \boldsymbol{x}_a) \qquad (1)$$

where y denotes the measured DSCDs, $\boldsymbol{F}(x, b)$ denotes the forward model, b

https://doi.org/10.5194/egusphere-2026-3286
Preprint. Discussion started: 1 July 2026

represents auxiliary parameters (e.g., temperature, atmospheric pressure, single scattering albedo, asymmetry factor), x_a is the constrained prior vector, S_ε is the covariance matrix of y, and S_a is the covariance matrix of x. For aerosols and trace gases, initial profiles were assumed to follow an exponential decrease with height, reflecting the typical rapid attenuation of boundary layer pollutants. As O_4 absorption is linked to aerosol optical properties, aerosol vertical profiles were retrieved from O_4 DSCDs at different elevation angles and used as input to derive vertical profiles of HONO, HCHO, and O_3. Different single scattering albedos (SSA) and asymmetry parameters were applied at the two sites (AHU: 0.90 and 0.69; CF: 0.92 and 0.60)(Xing et al., 2024a; Zou et al., 2025). Vertical profiles with relative retrieval errors > 50% or degrees of freedom (DOF) < 1.0 were excluded prior to analysis. Detailed error analysis for the vertical profile retrievals is provided in Section S1, with total errors of 24% (HONO), 33% (HCHO), and 22% (O_3), where smoothing and noise errors dominate (HONO:16%, HCHO:27%, O_3:8%).

2.3 TUV model

The Tropospheric Ultraviolet and Visible (TUV) radiation model, developed by the National Center for Atmospheric Research (NCAR) based on radiative transfer theory and implemented in FORTRAN, was used to simulate solar radiation transfer within the troposphere and calculate photolysis frequencies for key atmospheric reactions. In this study, the TUV model was applied to derive the photolysis rates of HONO, HCHO, and O_3. Model inputs were constrained using observational datasets. Aerosol optical depth (AOD) at ~361 nm was obtained from aerosol extinction vertical profiles retrieved from the ground-based hyperspectral remote sensing observations. Total column ozone was derived from daily TROPOMI satellite products, with values typically ranging from 260 to 280 DU. The SSA was retrieved from regression analyses of O_4 absorption features at 361 and 477 nm(Xing et al., 2019).

3. Results and discussion

3.1 Overview

Figure 2 presents the seasonal mean vertical profiles of HONO, HCHO, and O_3 at urban and rural sites in spring and summer 2023 (monthly mean profiles are shown in Figure S2-S3), revealing their urban-rural differences and seasonal evolution in the vertical direction. Two key aspects are evident: First, the stark contrast in near surface concentrations between urban and rural areas reflects the control of anthropogenic emissions and chemical titration. In spring, the near surface HONO concentration at the urban (AHU) site (0.11 ppb) was 1.6 times that at the rural (CF, 0.069 ppb) site and decayed rapidly with height, directly confirming the near surface confinement of strong point source emissions in cities. Conversely, near surface O_3 in the urban area was suppressed to 24 ppb in spring, far below the 57 ppb in the rural area, a 33 ppb gap that underscores the intense titration effect of fresh NO emissions on urban O_3. Second, seasonal vertical structural changes reflect the reshaping of gradients by photochemistry and boundary layer mixing. From spring to summer (Figure 3a5, b5, c5), near surface HONO in the urban area dropped sharply by 65% (to 0.039 ppb) with a gentler gradient, revealing the peak-shaving effect of strong photolysis and convective mixing(Crilley et al., 2019; Wong et al., 2011), while rural HONO showed no significant seasonal variation. Urban HCHO profiles transitioned from a sharp vertical decline in spring (primary emission dominated) to homogenization in summer (with obvious high values in the middle and upper layers, with a difference of less

https://doi.org/10.5194/egusphere-2026-3286
Preprint. Discussion started: 1 July 2026

than 30% from the ground), and summer middle and upper HCHO concentrations in urban areas were 56.3% higher than in rural areas, demonstrating that intense secondary photochemical formation penetrates the entire urban boundary layer. Additionally, urban O_3 exhibited a 55 ppb high-value zone (twice the surface level) at 0.5–0.8 km, whereas the rural boundary layer showed <10 ppb extreme variation, indicating urban O_3 is controlled by the superposition of photochemical formation and physical trapping by the inversion layer (Jaffe et al., 2018; Wang et al., 2018, 2022a), while the rural area is dominated by regional transport and thorough mixing. The vertical profile data confirm that the spring boundary layer is dominated by local primary emissions and near surface chemical titration; in summer, with intensified photochemistry and a rising boundary layer, pollutant vertical distributions homogenize, and significant secondary pollution accumulates in the urban middle and upper layers.

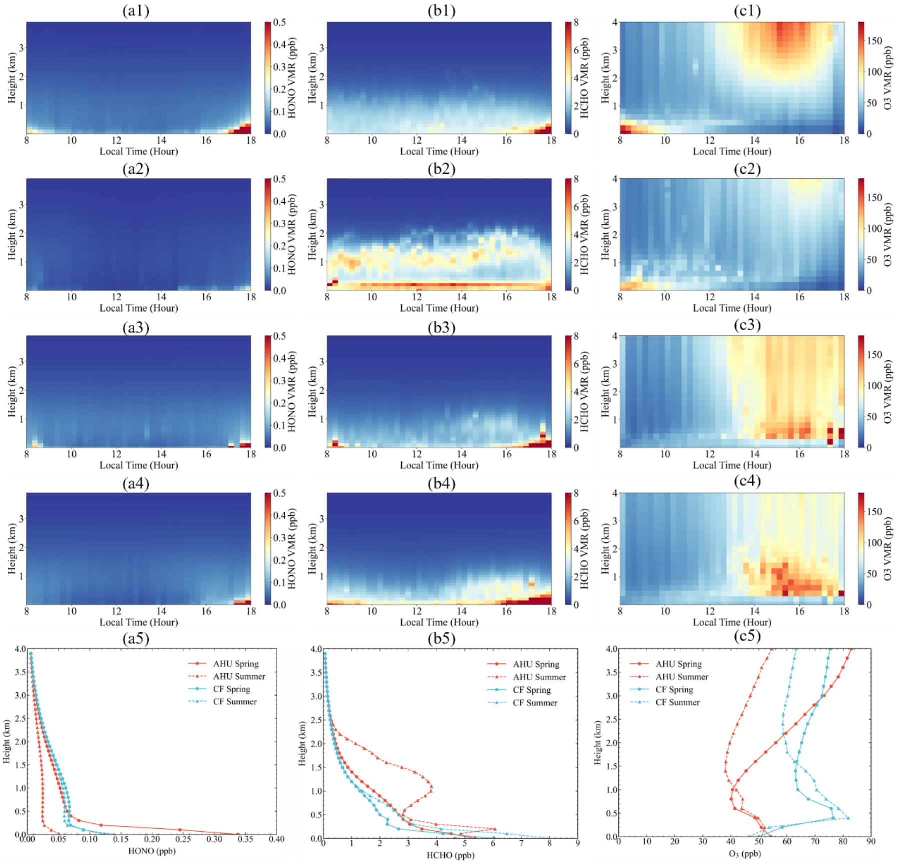

Figure 2. The first row (spring) and second row (summer) show the vertical profiles at the AHU site; the third row (spring) and fourth row (summer) show the vertical profiles at the CF site; the bottom row shows the seasonal mean vertical profiles. The left column represents HONO, the middle column represents HCHO, and the right column represents O_3.

3.2 Daytime HONO sources

3.2.1 Direct emission

https://doi.org/10.5194/egusphere-2026-3286
Preprint. Discussion started: 1 July 2026

Traffic direct emissions are a key source of HONO, particularly in traffic dense urban regions. To accurately quantify HONO secondary formation contributions, the impact of direct emissions must be excluded. Following established methods from prior research(Kramer et al., 2020; Li et al., 2021b; Liang et al., 2017), direct emission contributions were estimated via the linear relationship between ΔHONO and ΔNO_X (Figure S4). ΔHONO and ΔNO_X exhibited a strong correlation (R=0.75), with a mean $\Delta HONO/\Delta NO_x$ ratio of 0.79% ± 0.54%. At AHU site, HONO remaining after subtracting direct emissions accounted for ~76.8% of measured HONO: direct emissions contributed ~0.15 ppb HONO, while secondary formation contributed ~0.045 ppb, meaning direct emissions represented ~23.2% of total HONO, indicating secondary formation remains the primary HONO source in urban areas. Detailed data analysis procedures are provided in Section S2. At CF site, the absence of in-situ NO_X analysis data and the complexity of non-traditional sources (e.g., soil emissions) in agricultural areas led to categorizing direct emissions as unknown. In subsequent secondary source apportionment, this study focuses on dissecting HONO's heterogeneous formation mechanism by analyzing the vertical evolution of the $HONO/NO_2$ ratio and the NO_2-to-HONO conversion rate $C_{(HONO)}$.

3.2.2 Heterogeneous contribution to HONO

Abundant research confirms that in known daytime HONO sources, heterogeneous reactions of NO_2 on wet surfaces or aerosol surfaces typically contribute 50%–80%, making them a key source(Ryan et al., 2018; Zhang et al., 2022), whereas homogeneous reactions play a minor role and are excluded from this study(Yang et al., 2025). To elucidate heterogeneous formation differences across seasons and heights between urban and rural sites, we analyzed vertical profile retrieval characteristics of the $HONO/NO_2$ ratio and conversion rate $C_{(HONO)}$, a core indicator of NO_2 heterogeneous conversion potential. Seasonal mean data (Figure 3c, 3d) reveal a striking urban-rural seasonal reversal: in spring, the near surface $HONO/NO_2$ ratio at the urban AHU site (0.040) is significantly higher than at the rural CF site (0.026), aligning with the traditional view that urban areas have elevated NO_2 and aerosol surface areas. However, this pattern reverses entirely in summer: the AHU near surface ratio plummets to 0.012, while the CF ratio surges to 0.048 (nearly 4 times of the urban value).

This macroscopic seasonal shift is further mechanistically validated by monthly mean vertical data (Figure 3a, 3b). For the urban AHU site, the near surface (0–0.2 km) $HONO/NO_2$ ratio in summer (June to August) is extremely low (e.g., 0.008 in June and August), driven by rapid photolysis of near surface HONO under intense ultraviolet radiation(Cheng et al., 2025; He et al., 2023). Notably, AHU exhibits a unique deep valley vertical structure in summer: in August, the ratio is 0.008 near the surface, oscillates at low values in the 0.2–0.5 km layer, but rises sharply from 0.6 km, reaching 0.089 at 3.9 km. This structure indicates that urban summer near surface acts as a HONO sink due to strong titration and photolysis, while the boundary layer's middle and upper sections, enriched in aerosols (Figure S5) and shielded from near surface photolysis competition, become active zones for NO_2-to-HONO conversion. In contrast, the rural CF site shows a distinct vertical trend: in summer August, the near surface ratio is 0.069, increasing monotonically with altitude (0.069 to 0.100). This suggests heterogeneous conversion remains active from the surface to high altitude in rural areas. Coupled with the rural site's surface characteristics, this high ratio likely stems from increased soil moisture and ammonia release during summer agricultural activities (e.g., fertilization), which significantly enhance near surface

NO_2 heterogeneous conversion(Xing et al., 2024a; Xue et al., 2021).

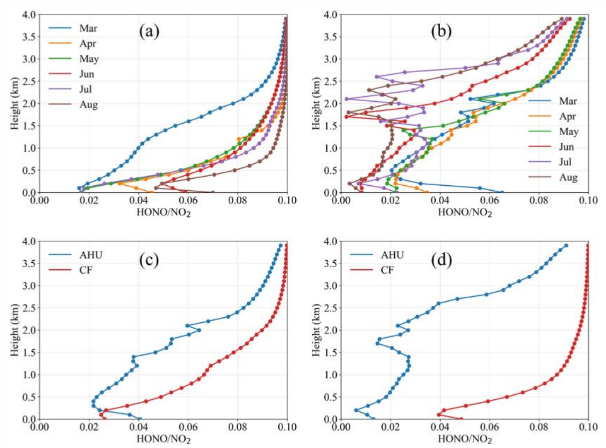

Figure 3. (a) $HONO/NO_2$ at CF from March to August, (b) $HONO/NO_2$ at AHU from March to August, (c) $HONO/NO_2$ in spring, and (d) $HONO/NO_2$ in summer.

To further translate these potentials into actual rates, we calculated the daytime NO_2-to-HONO conversion rate $C_{(HONO)}$ (Figure 4) using the formula(Wentzell et al., 2010; Xing et al., 2024a):

$$C_{(HONO)}=\frac{\frac{[HONO]_{t_2}}{[NO_2]_{t_2}}-\frac{[HONO]_{t_1}}{[NO_2]_{t_1}}}{t_2-t_1} \qquad (2)$$

Figure 4c presents seasonal data for $C_{(HONO)}$, which not only confirms the conclusions from the $HONO/NO_2$ ratio but also elucidates the vertical driving mechanisms of urban-rural atmospheric oxidizing capacity. In spring, $C_{(HONO)}$ at both sites exhibits typical exponential decay with height: the surface rate at AHU (0.054 h^{-1}) is slightly higher than at CF (0.048 h^{-1}), and both decrease to 0.028 h^{-1} and 0.031 h^{-1} at 1.0 km, respectively. This indicates that in spring, heterogeneous reactions are primarily anchored near the surface at both urban and rural sites, driven by local emissions and surface processes. However, summer data reveals a scientifically significant phenomenon: the vertical gradient of $C_{(HONO)}$ differs markedly between sites. At CF, summer surface $C_{(HONO)}$ shows explosive growth (0.100 h^{-1}, >2 times of spring values) but declines sharply with height, falling to 0.033 h^{-1} at 0.5 km and 0.024 h^{-1} at 1.0 km. Analyzing monthly data from CF (Fig. 4b) reveals these near surface peaks are driven by extreme events in specific months (e.g., 0.117 h^{-1} in April, 0.126 h^{-1} in June, 0.165 h^{-1} in August). These peaks align closely with the local agricultural fertilization cycle, as strong soil heterogeneous sources create a near surface reaction pool(Song et al., 2023b; Xue et al., 2021). However, due to HONO's short atmospheric lifetime, this surface generated HONO is poorly transported to high altitudes via vertical turbulence, resulting in a steep vertical decline in its conversion rate(Meng et al., 2020a).

In contrast to the surface dominated pattern at the CF site, the AHU site exhibited a distinct vertical spatial shift in summer. Seasonal mean data (Figure 4c) show that the surface $C_{(HONO)}$ at AHU in summer was extremely low (0.017 h^{-1}), yet the rate increased in the 0.5–1.7 km layer, peaking at 0.05 h^{-1} at 2.5 km and forming a significant elevated structure aloft. Monthly data further confirm this: in July, AHU's surface $C_{(HONO)}$ was 0.037 h^{-1}, rising to 0.043 h^{-1}at 1.5 km; in August, the surface rate was 0.008 h^{-1} but climbed steadily with height, reaching 0.053 h^{-1} at 2.5 km (Figure 4a). This unique elevated heterogeneous conversion in urban summer can be explained by physical and chemical mechanisms. First, intense convective mixing lifts urban emitted NO_2 and aerosols to the middle and upper boundary layer (0.5–2.0 km), where precursors accumulate due to the inversion or residual layer. Second, relative humidity and aerosol surface properties in the middle and upper boundary layer may favor NO_2 heterogeneous hydrolysis more than the near surface. Li et al.(Li et al., 2025c) noted in a coastal-inland island comparison that aerosols promote HONO formation aloft, and our data refine this: in inland urban environments (e.g., Hefei), strong near surface photochemistry suppresses observable $C_{(HONO)}$, shifting the true heterogeneous conversion to the middle and upper boundary layer via vertical transport.

In summary, the HONO/NO_2 ratio and $C_{(HONO)}$ rate reveal urban-rural differences in heterogeneous HONO formation. Rural areas (CF) show surface-dominated mechanisms, driven by strong agricultural surface sources with limited vertical extension; urban areas (AHU) shift to an elevated pattern, with near surface photolysis suppression, while the middle-upper boundary layer, due to precursor capture and favorable aerosol conditions, becomes the site of summer HONO and subsequent OH radical formation. This finding revises the traditional view that heterogeneous reactions are surface limited and provides key chemical evidence for urban high-altitude oxidizing capacity mechanisms.

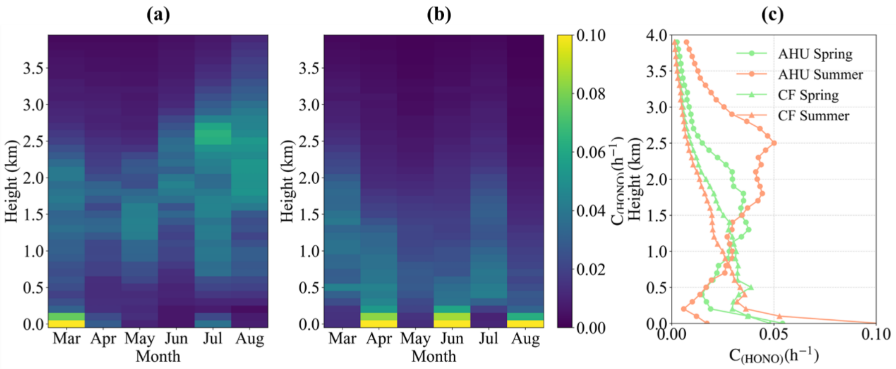

Figure 4. Monthly mean variations of $C_{(HONO)}$ at (a) AHU and (b) CF, and (c) seasonal mean $C_{(HONO)}$.

3.3 Daytime O_3 sources

Accurately determining the nonlinear response mechanism of O_3 formation is a prerequisite for understanding urban-rural differences in atmospheric oxidizing capacity. Tropospheric O_3 is not directly emitted but generated by complex photochemical reactions of NO_X and VOCs under light, exhibiting significant spatial heterogeneity in precursor sensitivity (VOCs-limited or NO_X-limited)(Wang et al., 2017, 2022b; Xue et al., 2026). As a key intermediate in VOCs photochemical oxidation, secondary HCHO has been widely used to assess O_3 formation sensitivity via its ratio with NO_2 (FNR). Here, we use linear fitting slopes of O_3 relative to normalized secondary HCHO (primary/secondary separation in Section S3) and NO_2 (S_{HCHO} and S_{NO2}) to define local chemical thresholds: the intersection of these slopes marks the transition zone, where S_{HCHO} dominated regions are VOCs-limited and S_{NO2} dominated regions are NO_X-limited(Li et al., 2024; Lin et al., 2022). The O_3

https://doi.org/10.5194/egusphere-2026-3286
Preprint. Discussion started: 1 July 2026

formation sensitivity thresholds are [1.48, 1.88] for AHU (Figure 5a1) and [1.04, 1.76] for CF (Figure 5b1).

Daytime FNR evolution data (Figure 5a2-a3, 5b2-b3) reveal seasonal and vertical differences in O_3 formation mechanisms between urban and rural areas. In spring, both sites transition from VOCs control to the transition zone, reflecting VOCs-limited photochemical cycles under low NO_X. In summer, strong photochemistry shifts the mechanism to NO_X control with vertical stratification: urban (AHU) 0–2 km is NO_X-limited, while 2–4 km shifts to VOCs control. This arises from a dual effect: extreme high temperature radiation accelerates VOCs-to-HCHO conversion, whereas fresh near surface NO_X emissions trigger intense O_3 titration, and their superposition causes severe NO_X limitation in the lower layer(Lu et al., 2018; Xue et al., 2026).

Rural (CF) areas show a more refined vertical structure in summer (0–1 km: NO_X-limited, 1–2.5 km: mixed control, 2.5–4 km: VOCs-limited, Figure 5b3). The stratification remains stable throughout the day, indicating dominance by large-scale thermodynamic boundary layer structures. In the lower layer, despite NO_2 enrichment, rapid consumption by strong photolysis and titration reactions imposes NO_X limitation. As height increases, NO_2 decays exponentially, while vertical transport of biogenic VOCs and their oxidation products slows HCHO decay. The middle layer reaches dynamic equilibrium (mixed limit), and the upper layer, with NO_2 dropping to background levels, fully transitions to VOCs control.

Overall, O_3 formation in spring is dominated by VOCs or mixed limit; strong photochemistry in summer reshapes the highly structured vertical gradient, the lower layer becomes severely NO_X-limited due to NO_X consumption, while the middle and upper layers shift to VOCs control as NO_2 decays and VOC oxidation products accumulate. This "lower layer NO_X, middle and upper layer VOCs" vertical chemical gradient signifies a fundamental reversal in the dominant OH radical formation pathways (lower layer: reliance on NO_2 photolysis; upper layer: reliance on HCHO photolysis). This discovery challenges the traditional flat surface observation paradigm and provides key observational constraints for developing three-dimensional atmospheric oxidation models.

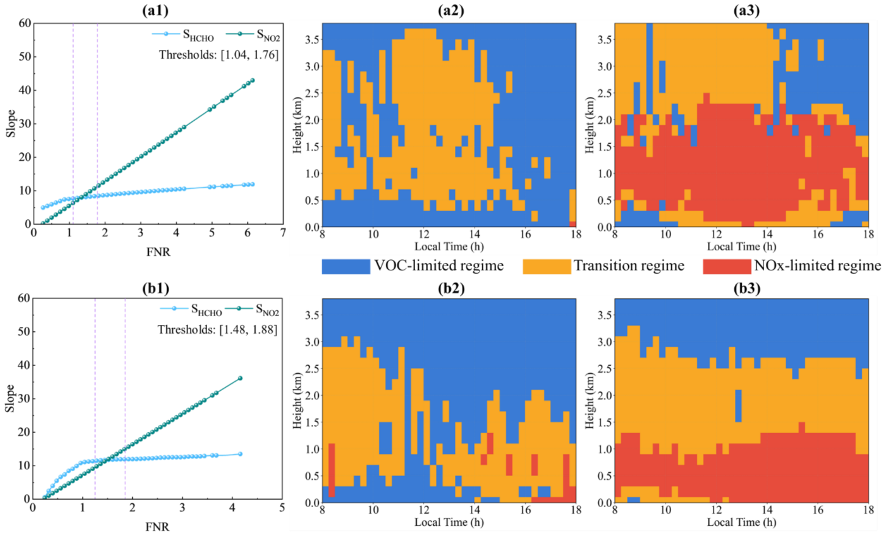

Figure 5. The first row shows AHU and the second row shows CF. The left column

shows the determination of O_3 control regime thresholds, the middle column shows O_3 formation sensitivity in spring, and the right column shows O_3 formation sensitivity in summer.

3.4 OH produced from HONO, HCHO and O_3

The core driving force of AOC is the generation of OH radicals. Daytime OH radicals primarily originate from the photolysis of O_3, direct photolysis of HONO, and photolysis of VOCs such as HCHO. Using observed vertical profiles of HONO, HCHO, and O_3, combined with photolysis rates from the TUV model, we quantitatively analyzed the vertical contributions of these three components to the OH radical formation rate (P(OH)) and their urban-rural seasonal differences. The OH radical production from HONO, HCHO, and O_3 is calculated via(Villena et al., 2011; Wang et al., 2010):

$$P(OH)_{HONO} = J(HONO) \times [HONO] \tag{3}$$

$$P(OH)_{HCHO} = 2 \times J(HCHO) \times [HCHO] \tag{4}$$

$$P(OH)_{O_3} = 2 \times f \times J(O(^1D)) \times [O_3] \tag{5}$$

Here, J(HONO), J(HCHO), and $J(O(^1D))$ denote the photolysis rates of HONO, HCHO, and O_3 (calculated by the TUV model); $O(^1D)$ is generated by O_3 photolysis, f represents the reaction $O(^1D) + H_2O \rightarrow 2OH$; [HONO], [HCHO], and $[O_3]$ are the concentrations of these species in different vertical layers.

Figure 6 presents the vertical profiles and diurnal variations of OH radical production rates from HONO, HCHO, and O_3 at AHU and CF sites in spring and summer. Notable seasonal and spatial variations exist in the sources and vertical structures of OH radical generation at urban and rural sites. At the urban AHU site, spring OH generation exhibits a pattern of "HONO dominated, HCHO secondary, O_3 minimal" (Figure 6a1-c1). The P(OH) driven by HONO is highly active near the surface (peaking at 4.43×10^{-4} ppb·s^{-1} at 18:00 on the ground) but decays exponentially with altitude, dropping to ~8.1×10^{-5} ppb·s^{-1} at 1.0 km, reflecting the influence of urban traffic primary emissions. The P(OH) of HCHO also peaks near the surface (~4.70×10^{-4} ppb·s^{-1}) and remains at 2.15×10^{-4} ppb·s^{-1} at 1.0 km, indicating contributions from near surface VOCs photochemistry. The P(OH) of O_3 is suppressed by NOx titration near the surface (~4.98×10^{-5} ppb·s^{-1}) but rises monotonically with altitude, increasing to 7.69×10^{-5} ppb·s^{-1} at 4.0 km (a >50% rise), signifying enhanced O_3 photolysis in the middle and upper atmosphere. In summer, the source structure of P(OH) at AHU undergoes a fundamental shift (Fig. 6a2-c2). The P(OH) driven by HONO is significantly weakened near the surface (peaking at ~1.65×10^{-4} ppb·s^{-1} at 18:00, a ~63% decrease from spring) but shows a relatively high-value zone in the 0.3–0.5 km layer (~4.78×10^{-5} - 5.17×10^{-5} ppb·s^{-1}), consistent with enhanced heterogeneous conversion aloft. The P(OH) driven by HCHO becomes the dominant source, with its near surface peak rising to 5.22×10^{-4} ppb·s^{-1} at 18:00 and a shallow vertical profile, remaining at 4.32×10^{-4} ppb·s^{-1} at 0.5–1.0 km (a <20% difference from the ground). This indicates that the large VOCs reaction pool in the urban area is highly active throughout the boundary layer in summer. The P(OH) of O_3 remains suppressed near the surface in summer (~5.20×10^{-5} ppb·s^{-1}), with a less steep vertical gradient of growth than in spring.

Rural CF exhibits distinct P(OH) characteristics (Figure 6a3-c4). HCHO driven P(OH) dominates in both seasons: its spring near surface peak is 1.63×10^{-3} ppb·s^{-1}, rising to 1.82×10^{-3} ppb·s^{-1} in summer (a ~12% increase), tightly linked to rural biogenic VOCs and their photochemical oxidation. The vertical profile drops rapidly

https://doi.org/10.5194/egusphere-2026-3286
Preprint. Discussion started: 1 July 2026

after the near surface peak, stabilizing above 1 km (~4.0×10^{-5} ppb·s^{-1}). HONO driven P(OH) is low, with spring and summer peaks of ~1.96×10^{-4} ppb·s^{-1} and ~2.17×10^{-4} ppb·s^{-1} (a ~11% increase), decaying quickly with height to approach the baseline above 2 km (~1.0×10^{-5} ppb·s^{-1}), reflecting weak rural sources. O_3 driven P(OH) increases monotonically: in spring, it rises from 2.0×10^{-5} ppb·s^{-1} (near surface, 18:00) to 9.15×10^{-5} ppb·s^{-1} (4 km, 358% increase), and in summer from 1.99×10^{-5} ppb·s^{-1} to 6.57×10^{-5} ppb·s^{-1} (230% increase). The larger spring vertical increase aligns with higher $O(^1D)$ and H_2O reaction efficiency under spring's relatively higher humidity.

Urban-rural contrasts reveal that in spring, AHU's OH generation depends on near surface primary emissions, with its $P(OH)_{HONO}$ peak 2.26 times CF's, reflecting strong urban traffic influence. Conversely, CF's OH is HCHO dominated, with its $P(OH)_{HCHO}$ peak 3.47 times AHU's, highlighting biogenic VOCs' role in rural oxidation. In summer, HCHO becomes AHU's core driver, expanding the oxidizing capacity's vertical influence from the near surface (spring) to the entire boundary layer. CF retains HCHO photolysis dominance, with its 11% summer near surface $P(OH)_{HCHO}$ increase contrasting AHU's 63% decrease, confirming rural summer soil heterogeneous sources. O_3 photolysis contributions rise with height at both sites, with greater relative impact at CF (especially spring high altitudes).

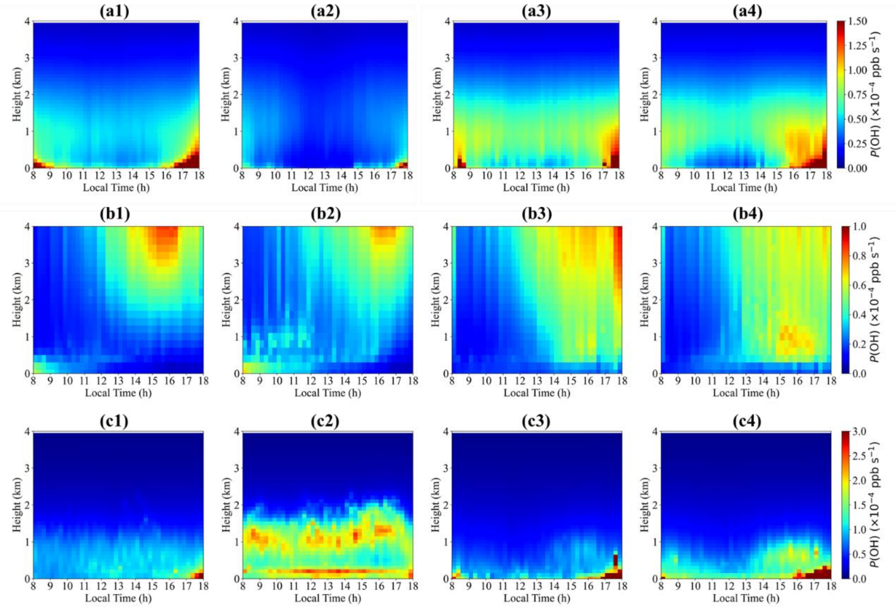

Figure 6. Production rates of OH radicals, P(OH). The top row represents HONO, the middle row represents O_3, and the bottom row represents HCHO. The first column shows AHU in spring, the second column shows CF in spring, the third column shows AHU in summer, and the fourth column shows CF in summer.

3.5 The Role of OH Radicals in Combined Air Pollution

AOC quantifies the atmosphere's ability to remove pollutants. The classical definition of AOC is the sum of the oxidation rates of all reducible species by all oxidants(Dai et al., 2023; Geyer et al., 2001). However, daytime OH radicals dominate this process due to their extremely high reactivity, accounting for over 90% of daytime atmospheric oxidizing capacity(Dai et al., 2023). With an extremely short

https://doi.org/10.5194/egusphere-2026-3286
Preprint. Discussion started: 1 July 2026

lifetime (<1 s), daytime OH radicals maintain a near-photochemical steady state between production and consumption. Here, we developed quantitative metrics for daytime atmospheric oxidizing potential (AOC_{day}) and pathway weight factors (W_i):

$$AOC_{day} = P(OH)_{total} = P(OH)_{HONO} + P(OH)_{HCHO} + P(OH)_{O3} \tag{6}$$

$$W_i = \frac{P(OH)_i}{AOC_{day}} \tag{7}$$

Figure 7 reveals the pronounced seasonal evolution and vertical stratification of the dominant pathways for OH radical generation from HCHO, HONO, and O_3. In spring, near surface driving mechanisms diverge between urban and rural sites. At the urban AHU site, AOC_{day} near the surface depends on primary emissions and early photochemical accumulation, with $P(OH)_{HONO}$ (4.43×10^{-4} ppb·s^{-1}) and $P(OH)_{HCHO}$ (4.70×10^{-4} ppb·s^{-1}) showing double peaks and weight factors of 45.6% and 47.2%, respectively, indicating urban oxidizing capacity is anchored near the surface. Conversely, the rural CF site's AOC_{day} is overwhelmingly dominated by HCHO photolysis, with its $P(OH)_{HCHO}$ peak (1.63×10^{-3} ppb·s^{-1}) ~3.47 times that of AHU, and W_{HCHO} reaching 67.9%, highlighting the strong role of rural biogenic VOCs oxidation. In summer, AHU's driving core shifts: W_{HONO} plummets from 45.6% to ~19%, while W_{HCHO} surges to 79.3% at 0.2 km, signaling the urban oxidation process extends throughout the boundary layer. Notably, urban W_{HONO} exhibits an anomalous rise of ~30.6% at 2.4 km, directly confirming the enhanced heterogeneous conversion aloft noted earlier. The rural CF site retains HCHO dominance, with near surface W_{HCHO} stabilizing at 72.5%; moreover, the 11% increase in its $P(OH)_{HONO}$ near the surface contrasts sharply with AHU's 63% decrease, validating the active role of rural soil heterogeneous sources near the surface. More significantly, both sites exhibit consistent vertical chemical stratification: at ~2.8 km, W_{O3} crosses the 50% threshold, reaching 74.3%–76.7% absolute dominance at 3.8 km. This reveals a vertically stratified oxidizing system: the lower layer (<1 km) is dominated by rapid oxidation via HCHO or HONO, while the middle and upper layers (>2.8 km) shift to O_3 photolysis dominance.

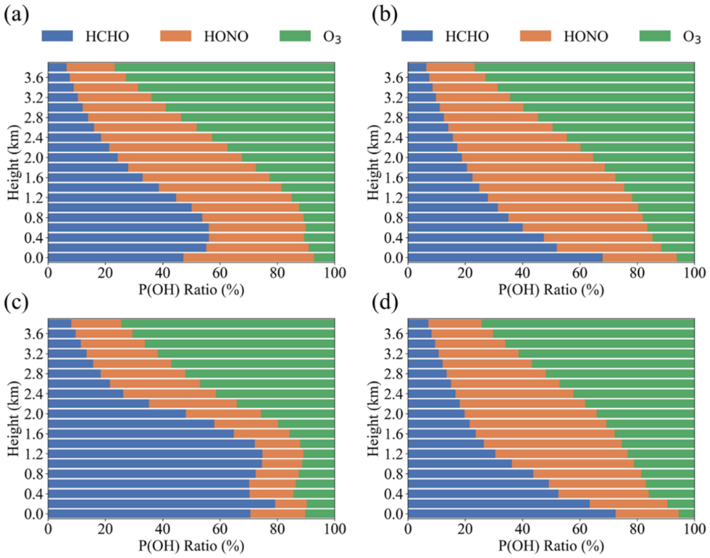

Figure 7. Contributions of HCHO, HONO, and O_3 to OH radical production rates P(OH) at different altitudes. The left column represents AHU and the right column represents CF. The top row shows spring and the bottom row shows summer.

Figure 8 presents the seasonal mean vertical distributions of AOC and aerosol in urban and rural areas during spring and summer. AOC exhibits a strong vertical correlation with aerosol (Figure S6, R = 0.88–0.93). Stronger AOC indicates stronger oxidizing capacity, facilitating the conversion of gaseous precursors to SOA and exacerbating air pollution, highlighting the central regulatory role of oxidizing capacity in pollution formation.

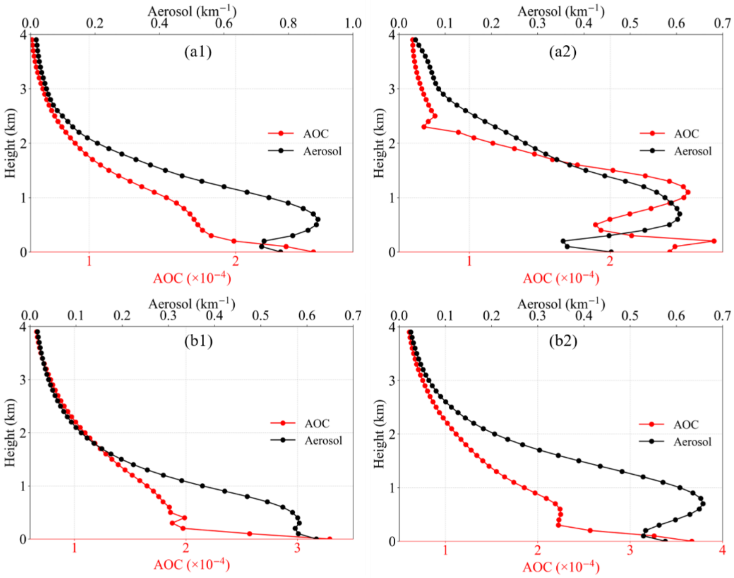

Figure 8. Comparison between seasonal mean vertical profiles of AOC and aerosols. The top row represents AHU and the bottom row represents CF. The left column shows spring and the right column shows summer.

Based on this metric, we propose three key constraints: (1) Urban O_3 control requires attention to vertical transport effects: simple reductions in surface NO_X may fail to improve O_3 due to high-altitude photochemical release and elevated HONO, consistent with the vertical dimension effects emphasized by Ivatt et al.(Ivatt et al., 2022). (2) Rural areas act as critical oxidizing reactors: their high HCHO driven oxidizing capacity indicates they are not only receptors but also sources of secondary precursors, necessitating regional coordinated emission reductions(Dai et al., 2023). (3) Vertical chemical stratification is a necessary constraint for refined models: breaking the flat-surface perception, three-dimensional models must accurately capture the vertical structure transitioning from HCHO dominated lower layers to O_3 dominated upper layers to assess high-altitude O_3 and SOA formation.

4.Conclusion

Using ground-based hyperspectral vertical remote sensing observations, this study reconstructs the vertical structure of AOC within the boundary layer. The central finding is the identification of a vertically stratified relay oxidation mechanism that is consistently observed across both urban and rural environments. First, both urban and rural atmospheres exhibited a clear vertical transition in oxidation regimes. Rapid oxidation below 1 km was primarily driven by HCHO and HONO, whereas O_3

photolysis became the dominant OH source above 2.8 km, contributing more than 74% of total OH production. This vertical partitioning challenges the long-standing paradigm—widely reported in previous studies from Beijing, Shanghai, and Guangzhou that intense oxidation and heterogeneous chemistry are confined to the near-surface atmosphere(He et al., 2023; Meng et al., 2020b). Second, the controlling OH production pathways displayed pronounced seasonal contrasts between urban and rural environments. In urban air masses, OH production shifted from near surface HONO dominance in spring ($P(OH)_{HONO}=4.43\times10^{-4}$ ppb·s^{-1}) to HCHO dominance in summer ($P(OH)_{HCHO}=5.22\times10^{-4}$ ppb·s^{-1}). Correspondingly, the HONO contribution decreased from 45.6% to 19%, whereas the HCHO contribution increased sharply to 79.3%. In rural regions, however, OH production remained strongly dominated by HCHO during both spring and summer ($P(OH)_{HCHO}=1.82\times10^{-3}$ ppb·s^{-1}), highlighting the role of rural atmospheres as active secondary pollutant reactors rather than passive pollutant receptors. This perspective has been largely underemphasized in previous regional assessments. Third, A particularly novel finding is the direct observational evidence of enhanced elevated HONO heterogeneous conversion within the urban boundary layer during summer. An anomalous HONO enhancement layer emerged near 2.4 km, where HONO contributed approximately 30.6% of OH production. Enhanced heterogeneous HONO conversion ($C_{(HONO)}$ = 0.053 h^{-1}) effectively shifted the dominant oxidation region from the photolysis-suppressed surface layer to the middle and upper boundary layer. By contrast, although near surface $C_{(HONO)}$ at the rural site reached 0.1 h^{-1} in summer, the conversion rate decreased sharply with altitude because of the short atmospheric lifetime of HONO.

Several caveats should be noted. First, the derived OH production rates rely on the radiative transfer parameterizations of the TUV model, which introduces inherent uncertainties. Second, the observations were restricted to the daytime boundary layer; consequently, nighttime oxidation processes and contributions from the free troposphere remain unquantified. Third, the spatial representativeness of this study is currently limited to the Yangtze–Huai River Basin.

These findings carry important implications. For atmospheric chemistry modeling, three-dimensional chemical transport models that neglect the vertical transition of OH production pathways are likely to underestimate the formation potential of elevated O_3 and secondary organic aerosols. For air quality management, our results provide a mechanistic explanation for the limited effectiveness of surface-only NOx mitigation strategies: persistent oxidation aloft, vertically decoupled photochemistry, and elevated HONO layers may collectively offset the benefits of emission reductions based solely on surface observations. Future regional pollution control strategies should integrate vertically resolved AOC diagnostics into both model development and regulatory design.

Declaration of Interest Statement

The authors declare that they have no known competing financial interests or personal relationships that could have appeared to influence the work reported in this paper.

Author Contributions Statement

Tiliang Zou: Conceptualization, Methodology, Data curation, Writing - original draft, Writing - review & editing, Resources. Chengzhi Xing: Methodology, Data curation, Resources, Writing - review & editing, Supervision. Zhijian Tang: Data curation, Formal analysis, Validation. Yikai Li: Formal analysis, Validation. Zhenyi Chen: Data curation, Formal analysis. Xiao Liang: Formal analysis, Validation. Wei Tan: Data curation, Validation. Cheng Liu: Resources, Review & editing, Supervision, Funding acquisition.

Financial support

This work was supported by the National Natural Science Foundation of China (42225504).

References

Cheng, P., Ling, J., Gong, Y., Yang, W., Wang, S., Han, B., Li, X., Yuan, B., Pei, C., Shen, J., Yu, Y., Huang, L., Deng, H., and Liu, Z.: Understanding Nitrous Acid (HONO) in the Urban Boundary Layer Using Continuous HONO Measurements at a 450 m Tall Tower in Guangzhou, China, Environ. Sci. Technol., 59, 10411–10421, https://doi.org/10.1021/acs.est.4c14279, 2025.

Crilley, L. R., Kramer, L. J., Ouyang, B., Duan, J., Zhang, W., Tong, S., Ge, M., Tang, K., Qin, M., Xie, P., Shaw, M. D., Lewis, A. C., Mehra, A., Bannan, T. J., Worrall, S. D., Priestley, M., Bacak, A., Coe, H., Allan, J., Percival, C. J., Popoola, O. A. M., Jones, R. L., and Bloss, W. J.: Intercomparison of nitrous acid (HONO) measurement techniques in a megacity (Beijing), Atmospheric Measurement Techniques, 12, 6449–6463, https://doi.org/10.5194/amt-12-6449-2019, 2019.

Dai, J., Brasseur, G. P., Vrekoussis, M., Kanakidou, M., Qu, K., Zhang, Y., Zhang, H., and Wang, T.: The atmospheric oxidizing capacity in China – Part 1: Roles of different photochemical processes, Atmospheric Chemistry and Physics, 23, 14127–14158, https://doi.org/10.5194/acp-23-14127-2023, 2023.

Fiore, A. M., Mickley, L. J., Zhu, Q., and Baublitz, C. B.: Climate and Tropospheric Oxidizing Capacity, Annual Review of Earth and Planetary Sciences, 52, 321–349, https://doi.org/10.1146/annurev-earth-032320-090307, 2024.

Geyer, A., Alicke, B., Konrad, S., Schmitz, T., Stutz, J., and Platt, U.: Chemistry and oxidation capacity of the nitrate radical in the continental boundary layer near Berlin, Journal of Geophysical Research: Atmospheres, 106, 8013–8025, https://doi.org/10.1029/2000JD900681, 2001.

He, S., Wang, S., Zhang, S., Zhu, J., Sun, Z., Xue, R., and Zhou, B.: Vertical distributions of atmospheric HONO and the corresponding OH radical production by photolysis at the suburb area of Shanghai, China, Science of The Total Environment, 858, 159703, https://doi.org/10.1016/j.scitotenv.2022.159703, 2023.

Ivatt, P. D., Evans, M. J., and Lewis, A. C.: Suppression of surface ozone by an aerosol-inhibited photochemical ozone regime, Nat. Geosci., 15, 536–540, https://doi.org/10.1038/s41561-022-00972-9, 2022.

Jaffe, D. A., Cooper, O. R., Fiore, A. M., Henderson, B. H., Tonnesen, G. S., Russell, A. G., Henze, D. K., Langford, A. O., Lin, M., and Moore, T.: Scientific assessment of background ozone over the U.S.: Implications for air quality management, Elementa: Science of the Anthropocene, 6, 56, https://doi.org/10.1525/elementa.309, 2018.

Kramer, L. J., Crilley, L. R., Adams, T. J., Ball, S. M., Pope, F. D., and Bloss, W. J.: Nitrous acid (HONO) emissions under real-world driving conditions from vehicles in a UK road tunnel, Atmospheric Chemistry and Physics, 20, 5231–5248, https://doi.org/10.5194/acp-20-5231-2020, 2020.

Kreher, K., Van Roozendael, M., Hendrick, F., Apituley, A., Dimitropoulou, E., Frieß, U., Richter, A., Wagner, T., Lampel, J., Abuhassan, N., Ang, L., Anguas, M., Bais, A., Benavent, N., Bösch, T., Bognar, K., Borovski, A., Bruchkouski, I., Cede, A., Chan, K. L., Donner, S., Drosoglou, T., Fayt, C., Finkenzeller, H., Garcia-Nieto, D., Gielen, C., Gómez-Martín, L., Hao, N., Henzing, B., Herman, J. R., Hermans, C., Hoque, S., Irie, H., Jin, J., Johnston, P., Khayyam Butt, J., Khokhar, F., Koenig, T. K., Kuhn, J., Kumar, V., Liu, C., Ma, J., Merlaud, A., Mishra, A. K., Müller, M., Navarro-Comas, M., Ostendorf, M., Pazmino, A., Peters, E., Pinardi, G., Pinharanda, M., Piters, A., Platt, U., Postylyakov, O., Prados-Roman, C., Puentedura, O., Querel, R., Saiz-Lopez, A., Schönhardt, A., Schreier, S. F., Seyler, A., Sinha, V., Spinei, E., Strong, K., Tack, F., Tian, X., Tiefengraber, M., Tirpitz, J.-L., van Gent, J., Volkamer, R., Vrekoussis, M., Wang, S., Wang, Z., Wenig, M., Wittrock, F., Xie, P. H., Xu, J., Yela, M., Zhang, C., and Zhao, X.: Intercomparison of NO_2, O_4, O_3 and HCHO slant column measurements by MAX-DOAS and zenith-sky UV–visible spectrometers during CINDI-2, Atmospheric Measurement Techniques, 13, 2169–2208, https://doi.org/10.5194/amt-13-2169-2020, 2020.

Lelieveld, J., Klingmüller, K., Pozzer, A., Burnett, R. T., Haines, A., and Ramanathan, V.: Effects of fossil fuel and total anthropogenic emission removal on public health and climate, Proceedings of the National Academy of Sciences of the United States of America, 116, 7192–7197, https://doi.org/10.1073/pnas.1819989116, 2019.

Li J., Liu Zhengyang., Yan Y., Song Y., Tang W., Yang L. I., Lin Z., Xiongfeng Z., Yulin H., and Fang B. I.: Short-Term Study on PAN and HONO Pollution Characteristics and Influencing Factors in Huizhou, Guangdong Province, hjkxyj, 38, 1011–1022, https://doi.org/10.13198/j.issn.1001-6929.2025.03.14, 2025a.

Li, K., Jacob, D. J., Liao, H., Qiu, Y., Shen, L., Zhai, S., Bates, K. H., Sulprizio, M. P., Song, S., Lu, X., Zhang, Q., Zheng, B., Zhang, Y., Zhang, J., Lee, H. C., and Kuk, S. K.: Ozone pollution in the North China Plain spreading into the late-winter haze season, Proc Natl Acad Sci U S A, 118, e2015797118, https://doi.org/10.1073/pnas.2015797118, 2021a.

Li, S., Song, W., Zhan, H., Zhang, Y., Zhang, X., Li, W., Tong, S., Pei, C., Wang, Y., Chen, Y., Huang, Z., Zhang, R., Zhu, M., Fang, H., Wu, Z., Wang, J., Luo, S., Fu, X., Xiao, S., Huang, X., Zeng, J., Zhang, H., Chen, D., Gligorovski, S., Ge, M., George, C., and Wang, X.: Contribution of Vehicle Emission and NO2 Surface Conversion to Nitrous Acid (HONO) in Urban Environments: Implications from Tests in a Tunnel, Environ. Sci. Technol., 55, 15616–15624, https://doi.org/10.1021/acs.est.1c00405, 2021b.

Li, Y., Xing, C., Hong, Q., Jiao, P., Peng, H., Tang, Z., and Liu, C.: Ozone Formation Sensitivity at Various Altitudes: Seeking the Optimal Method for Sensitivity Threshold Determination, Environ. Sci. Technol. Lett., 11, 1334–1339, https://doi.org/10.1021/acs.estlett.4c00777, 2024.

Li, Y., Xing, C., Chen, J., Jiao, P., Liu, C., Fang, J., and Liu, C.: Hyperspectral Imaging Technology Empowering Dynamic Monitoring of VOCs: A Breakthrough High-Spatial-Temporal Resolution Detection Method, Anal. Chem., 97, 13840–13849, https://doi.org/10.1021/acs.analchem.5c00837, 2025b.

Li, Y., Xing, C., Peng, H., Jiao, P., Zhang, Q., Liu, C., Sun, Z., Tan, W., and Liu, C.: Vertical Differences in NO2-to-HONO Heterogeneous Conversion and HONO-Driven OH Production over Inland, Coastal, and Island Regions, Environ. Sci. Technol., 59, 26020–26030, https://doi.org/10.1021/acs.est.5c10318, 2025c.

Liang, Y., Zha, Q., Wang, W., Cui, L., Lui, K. H., Ho, K. F., Wang, Z., Lee, S., and Wang, T.: Revisiting nitrous acid (HONO) emission from on-road vehicles: A tunnel study with a mixed fleet, Journal of the Air & Waste Management Association, 67, 797–805, https://doi.org/10.1080/10962247.2017.1293573, 2017.

Liao, Z., Gao, M., Zhang, J., Sun, J., Quan, J., Jia, X., Pan, Y., and Fan, S.:

Mixing-layer-height-referenced ozone vertical distribution in the lower troposphere of Chinese megacities: stratification, classification, and meteorological and photochemical mechanisms, Atmospheric Chemistry and Physics, 24, 3541–3557, https://doi.org/10.5194/acp-24-3541-2024, 2024.

Lin, H., Xing, C., Hong, Q., Liu, C., Ji, X., Liu, T., Lin, J., Lu, C., Tan, W., Li, Q., and Liu, H.: Diagnosis of Ozone Formation Sensitivities in Different Height Layers via MAX-DOAS Observations in Guangzhou, Journal of Geophysical Research: Atmospheres, 127, e2022JD036803, https://doi.org/10.1029/2022JD036803, 2022.

Liu, C., Xing, C., Hu, Q., Li, Q., Liu, H., Hong, Q., Tan, W., Ji, X., Lin, H., Lu, C., Lin, J., Liu, H., Wei, S., Chen, J., Yang, K., Wang, S., Liu, T., and Chen, Y.: Ground-Based Hyperspectral Stereoscopic Remote Sensing Network: A Promising Strategy to Learn Coordinated Control of O3 and PM2.5 over China, Engineering, 19, 71–83, https://doi.org/10.1016/j.eng.2021.02.019, 2022a.

Liu, D., Wang, M., Hu, K., Liu, Z., Dong, H., Zhang, B., Zhao, X., and Ji, W.: Sources and budget analysis of ambient formaldehyde in the east-central area of the yangtze River Delta region, China, Atmospheric Environment, 305, 119801, https://doi.org/10.1016/j.atmosenv.2023.119801, 2023.

Liu, T., Hong, Y., Li, M., Xu, L., Chen, J., Bian, Y., Yang, C., Dan, Y., Zhang, Y., Xue, L., Zhao, M., Huang, Z., and Wang, H.: Atmospheric oxidation capacity and ozone pollution mechanism in a coastal city of southeastern China: analysis of a typical photochemical episode by an observation-based model, Atmospheric Chemistry and Physics, 22, 2173–2190, https://doi.org/10.5194/acp-22-2173-2022, 2022b.

Lu, K., Fuchs, H., Hofzumahaus, A., Tan, Z., Wang, H., Zhang, L., Schmitt, S. H., Rohrer, F., Bohn, B., Broch, S., Dong, H., Gkatzelis, G. I., Hohaus, T., Holland, F., Li, X., Liu, Y., Liu, Y., Ma, X., Novelli, A., Schlag, P., Shao, M., Wu, Y., Wu, Z., Zeng, L., Hu, M., Kiendler-Scharr, A., Wahner, A., and Zhang, Y.: Fast Photochemistry in Wintertime Haze: Consequences for Pollution Mitigation Strategies, Environ Sci Technol, 53, 10676–10684, https://doi.org/10.1021/acs.est.9b02422, 2019.

Lu, K. D., Hofzumahaus, A., Holland, F., Bohn, B., Brauers, T., Fuchs, H., Hu, M., Häseler, R., Kita, K., Kondo, Y., Li, X., Lou, S. R., Oebel, A., Shao, M., Zeng, L. M., Wahner, A., Zhu, T., Zhang, Y. H., and Rohrer, F.: Missing OH source in a suburban environment near Beijing: observed and modelled OH and HO_2 concentrations in summer 2006, Atmospheric Chemistry and Physics, 13, 1057–1080, https://doi.org/10.5194/acp-13-1057-2013, 2013.

Lu, X., Hong, J., Zhang, L., Cooper, O. R., Schultz, M. G., Xu, X., Wang, T., Gao, M., Zhao, Y., and Zhang, Y.: Severe Surface Ozone Pollution in China: A Global Perspective, Environ. Sci. Technol. Lett., 5, 487–494, https://doi.org/10.1021/acs.estlett.8b00366, 2018.

Mao, J., Jacob, D. J., Evans, M. J., Olson, J. R., Ren, X., Brune, W. H., Clair, J. M. S., Crounse, J. D., Spencer, K. M., Beaver, M. R., Wennberg, P. O., Cubison, M. J., Jimenez, J. L., Fried, A., Weibring, P., Walega, J. G., Hall, S. R., Weinheimer, A. J., Cohen, R. C., Chen, G., Crawford, J. H., McNaughton, C., Clarke, A. D., Jaeglé, L., Fisher, J. A., Yantosca, R. M., Le Sager, P., and Carouge, C.: Chemistry of hydrogen oxide radicals (HO_x) in the Arctic troposphere in spring, Atmospheric Chemistry and Physics, 10, 5823–5838, https://doi.org/10.5194/acp-10-5823-2010, 2010.

Meng, F., Qin, M., Tang, K., Duan, J., Fang, W., Liang, S., Ye, K., Xie, P., Sun, Y., Xie, C., Ye, C., Fu, P., Liu, J., and Liu, W.: High-resolution vertical distribution and sources of HONO and NO_2 in the nocturnal boundary layer in urban Beijing, China, Atmospheric Chemistry and Physics, 20, 5071–5092, https://doi.org/10.5194/acp-20-5071-2020, 2020a.

Meng, F., Qin, M., Tang, K., Duan, J., Fang, W., Liang, S., Ye, K., Xie, P., Sun, Y., Xie, C., Ye, C., Fu, P., Liu, J., and Liu, W.: High-resolution vertical distribution and sources of HONO and NO_2 in the nocturnal boundary layer in urban Beijing, China, Atmospheric Chemistry and Physics, 20, 5071–5092, https://doi.org/10.5194/acp-20-5071-2020, 2020b.

Monks, P. S., Granier, C., Fuzzi, S., Stohl, A., Williams, M. L., Akimoto, H., Amann, M., Baklanov, A., Baltensperger, U., Bey, I., Blake, N., Blake, R. S., Carslaw, K., Cooper, O. R., Dentener, F., Fowler, D., Fragkou, E., Frost, G. J., Generoso, S., Ginoux, P., Grewe, V., Guenther, A., Hansson, H. C., Henne, S., Hjorth, J., Hofzumahaus, A., Huntrieser, H., Isaksen, I. S. A., Jenkin, M. E., Kaiser, J., Kanakidou, M., Klimont, Z., Kulmala, M., Laj, P., Lawrence, M. G., Lee, J. D., Liousse, C., Maione, M., McFiggans, G., Metzger, A., Mieville, A., Moussiopoulos, N., Orlando, J. J., O'Dowd, C. D., Palmer, P. I., Parrish, D. D., Petzold, A., Platt, U., Pöschl, U., Prévôt, A. S. H., Reeves, C. E., Reimann, S., Rudich, Y., Sellegri, K., Steinbrecher, R., Simpson, D., ten Brink, H., Theloke, J., van der Werf, G. R., Vautard, R., Vestreng, V., Vlachokostas, Ch., and von Glasow, R.: Atmospheric composition change – global and regional air quality, Atmospheric Environment, 43, 5268–5350, https://doi.org/10.1016/j.atmosenv.2009.08.021, 2009.

Monks, P. S., Archibald, A. T., Colette, A., Cooper, O., Coyle, M., Derwent, R., Fowler, D., Granier, C., Law, K. S., Mills, G. E., Stevenson, D. S., Tarasova, O., Thouret, V., von Schneidemesser, E., Sommariva, R., Wild, O., and Williams, M. L.: Tropospheric ozone and its precursors from the urban to the global scale from air quality to short-lived climate forcer, Atmospheric Chemistry and Physics, 15, 8889–8973, https://doi.org/10.5194/acp-15-8889-2015, 2015.

Nan, J., Wang, S., Guo, Y., Xiang, Y., and Zhou, B.: Study on the daytime OH radical and implication for its relationship with fine particles over megacity of Shanghai, China, Atmospheric Environment, 154, 167–178, https://doi.org/10.1016/j.atmosenv.2017.01.046, 2017.

Pan, Y., Xiang, Y., Pei, C., Lv, L., Chen, Z., Liu, W., and Zhang, T.: Vertical distribution and transport characteristics of ozone pollution based on lidar observation network and data assimilation over the Pearl River Delta, China, Atmospheric Research, 310, 107643, https://doi.org/10.1016/j.atmosres.2024.107643, 2024.

Price, P., Bottorff, B., Jenkins, J., Brune, W. H., and Stevens, P. S.: Re-assessing hydroxyl radical chemistry in the atmosphere: Instrument interferences may explain previous measurement discrepancies, Commun Earth Environ, 6, 325, https://doi.org/10.1038/s43247-025-02308-y, 2025.

Ran, H., An, J., Zhang, J., Huang, J., Qu, Y., Chen, Y., Xue, C., Mu, Y., and Liu, X.: Impact of soil–atmosphere HONO exchange on concentrations of HONO and O3 in the North China Plain, Science of The Total Environment, 928, 172336, https://doi.org/10.1016/j.scitotenv.2024.172336, 2024.

Ren, B., Xie, P., Xu, J., Li, A., Qin, M., Hu, R., Zhang, T., Fan, G., Tian, X., Zhu, W., Hu, Z., Huang, Y., Li, X., Meng, F., Zhang, G., Tong, J., Ren, H., Zheng, J., Zhang, Z., and Lv, Y.: Vertical characteristics of NO2 and HCHO, and the ozone formation regimes in Hefei, China, Science of The Total Environment, 823, 153425, https://doi.org/10.1016/j.scitotenv.2022.153425, 2022.

Ryan, R. G., Rhodes, S., Tully, M., Wilson, S., Jones, N., Frieß, U., and Schofield, R.: Daytime HONO, NO_2 and aerosol distributions from MAX-DOAS observations in Melbourne, Atmospheric Chemistry and Physics, 18, 13969–13985, https://doi.org/10.5194/acp-18-13969-2018, 2018.

Sahu, S. K., Liu, S., Liu, S., Ding, D., and Xing, J.: Ozone pollution in China: Background and transboundary contributions to ozone concentration & related health effects across the country, Science of The Total Environment, 761, 144131, https://doi.org/10.1016/j.scitotenv.2020.144131, 2021.

Shen, Y., Wang, Y., Cheng, M., and Tang, G.: Critical role of vertical exchange in the boundary layer on urban photochemical pollution, Science of The Total Environment, 987, 179779, https://doi.org/10.1016/j.scitotenv.2025.179779, 2025.

Song, Y., Xing, C., Liu, C., Lin, J., Wu, H., Liu, T., Lin, H., Zhang, C., Tan, W., Ji, X., Liu, H., and Li, Q.: Evaluation of transport processes over North China Plain and Yangtze River Delta using MAX-DOAS observations, Atmospheric Chemistry and Physics, 23, 1803–1824, https://doi.org/10.5194/acp-23-1803-2023, 2023a.

Song, Y., Xue, C., Zhang, Y., Liu, P., Bao, F., Li, X., and Mu, Y.: Measurement report: Exchange fluxes of HONO over agricultural fields in the North China Plain, Atmospheric Chemistry and Physics, 23, 15733–15747, https://doi.org/10.5194/acp-23-15733-2023, 2023b.

Spurr, R. J. D.: VLIDORT: A linearized pseudo-spherical vector discrete ordinate radiative transfer code for forward model and retrieval studies in multilayer multiple scattering media, Journal of Quantitative Spectroscopy and Radiative Transfer, 102, 316–342, https://doi.org/10.1016/j.jqsrt.2006.05.005, 2006.

Tan, Z., Lu, K., Jiang, M., Su, R., Wang, H., Lou, S., Fu, Q., Zhai, C., Tan, Q., Yue, D., Chen, D., Wang, Z., Xie, S., Zeng, L., and Zhang, Y.: Daytime atmospheric oxidation capacity in four Chinese megacities during the photochemically polluted season: a case study based on box model simulation, Atmospheric Chemistry and Physics, 19, 3493–3513, https://doi.org/10.5194/acp-19-3493-2019, 2019.

Villena, G., Wiesen, P., Cantrell, C. A., Flocke, F., Fried, A., Hall, S. R., Hornbrook, R. S., Knapp, D., Kosciuch, E., Mauldin, R. L., McGrath, J. A., Montzka, D., Richter, D., Ullmann, K., Walega, J., Weibring, P., Weinheimer, A., Staebler, R. M., Liao, J., Huey, L. G., and Kleffmann, J.: Nitrous acid (HONO) during polar spring in Barrow, Alaska: A net source of OH radicals?, Journal of Geophysical Research: Atmospheres, 116, https://doi.org/10.1029/2011JD016643, 2011.

Vo, T.-D.-H., Lin, C., Weng, C.-E., Yuan, C.-S., Lee, C.-W., Hung, C.-H., Bui, X.-T., Lo, K.-C., and Lin, J.-X.: Vertical stratification of volatile organic compounds and their photochemical product formation potential in an industrial urban area, Journal of Environmental Management, 217, 327–336, https://doi.org/10.1016/j.jenvman.2018.03.101, 2018.

Wang, Q., Sun, Y., Xu, W., Du, W., Zhou, L., Tang, G., Chen, C., Cheng, X., Zhao, X., Ji, D., Han, T., Wang, Z., Li, J., and Wang, Z.: Vertically resolved characteristics of air pollution during two severe winter haze episodes in urban Beijing, China, Atmospheric Chemistry and Physics, 18, 2495–2509, https://doi.org/10.5194/acp-18-2495-2018, 2018.

Wang, T., Xue, L., Brimblecombe, P., Lam, Y. F., Li, L., and Zhang, L.: Ozone pollution in China: A review of concentrations, meteorological influences, chemical precursors, and effects, Science of the Total Environment, 575, 1582–1596, https://doi.org/10.1016/j.scitotenv.2016.10.081, 2017.

Wang, T., Xue, L., Feng, Z., Dai, J., Zhang, Y., and Tan, Y.: Ground-level ozone pollution in China: a synthesis of recent findings on influencing factors and impacts, Environ. Res. Lett., 17, 063003, https://doi.org/10.1088/1748-9326/ac69fe, 2022a.

Wang, X., Wang, H., and Wang, S.: Ambient formaldehyde and its contributing factor to ozone and OH radical in a rural area, Atmospheric Environment, 44, 2074–2078, https://doi.org/10.1016/j.atmosenv.2010.03.023, 2010.

Wang, Y., Apituley, A., Bais, A., Beirle, S., Benavent, N., Borovski, A., Bruchkouski, I., Chan, K. L., Donner, S., Drosoglou, T., Finkenzeller, H., Friedrich, M. M., Frieß, U., Garcia-Nieto, D., Gómez-Martín, L., Hendrick, F., Hilboll, A., Jin, J., Johnston, P., Koenig, T. K., Kreher, K., Kumar, V., Kyuberis, A., Lampel, J., Liu, C., Liu, H., Ma, J., Polyansky, O. L., Postylyakov, O., Querel, R., Saiz-Lopez, A., Schmitt, S., Tian, X., Tirpitz, J.-L., Van Roozendael, M., Volkamer, R., Wang, Z., Xie, P., Xing, C., Xu, J., Yela, M., Zhang, C., and Wagner, T.: Inter-comparison of MAX-DOAS measurements of tropospheric HONO slant column densities and vertical profiles during the CINDI-2 campaign, Atmospheric Measurement Techniques, 13, 5087–5116, https://doi.org/10.5194/amt-13-5087-2020, 2020.

Wentzell, J. J. B., Schiller, C. L., and Harris, G. W.: Measurements of HONO during BAQS-Met, Atmospheric Chemistry and Physics, 10, 12285–12293, https://doi.org/10.5194/acp-10-12285-2010, 2010.

Wolfe, G. M., Nicely, J. M., St. Clair, J. M., Hanisco, T. F., Liao, J., Oman, L. D., Brune, W. B., Miller, D., Thames, A., González Abad, G., Ryerson, T. B., Thompson, C. R., Peischl, J., McKain, K., Sweeney, C., Wennberg, P. O., Kim, M., Crounse, J. D., Hall, S. R., Ullmann, K., Diskin, G., Bui, P., Chang, C., and Dean-Day, J.: Mapping hydroxyl variability throughout the global remote troposphere via synthesis of airborne and satellite formaldehyde observations, Proceedings of the National Academy of Sciences, 116, 11171–11180, https://doi.org/10.1073/pnas.1821661116, 2019.

Wong, K. W., Oh, H.-J., Lefer, B. L., Rappenglück, B., and Stutz, J.: Vertical profiles of nitrous acid in the nocturnal urban atmosphere of Houston, TX, Atmospheric Chemistry and Physics, 11, 3595–3609, https://doi.org/10.5194/acp-11-3595-2011, 2011.

Wu, Y., Huo, J., Yang, G., Wang, Y., Wang, L., Wu, S., Yao, L., Fu, Q., and Wang, L.: Measurement report: Production and loss of atmospheric formaldehyde at a suburban site of Shanghai in summertime, Atmospheric Chemistry and Physics, 23, 2997–3014, https://doi.org/10.5194/acp-23-2997-2023, 2023.

Xing, C., Liu, C., Wang, S., Chan, K. L., Gao, Y., Huang, X., Su, W., Zhang, C., Dong, Y., Fan, G., Zhang, T., Chen, Z., Hu, Q., Su, H., Xie, Z., and Liu, J.: Observations of the vertical distributions of summertime atmospheric pollutants and the corresponding ozone production in Shanghai, China, Atmospheric Chemistry and Physics, 17, 14275–14289, https://doi.org/10.5194/acp-17-14275-2017, 2017.

Xing, C., Liu, C., Wang, S., Hu, Q., Liu, H., Tan, W., Zhang, W., Li, B., and Liu, J.: A new method to determine the aerosol optical properties from multiple-wavelength O_4 absorptions by MAX-DOAS observation, Atmospheric Measurement Techniques, 12, 3289–3302, https://doi.org/10.5194/amt-12-3289-2019, 2019.

Xing, C., Xu, S., Song, Y., Liu, C., Liu, Y., Lu, K., Tan, W., Zhang, C., Hu, Q., Wang, S., Wu, H., and Lin, H.: A new insight into the vertical differences in NO_2 heterogeneous reaction to produce HONO over inland and marginal seas, Atmospheric Chemistry and Physics, 23, 5815–5834, https://doi.org/10.5194/acp-23-5815-2023, 2023.

Xing, C., Liu, C., Li, Q., Wang, S., Tan, W., Zou, T., Wang, Z., and Lu, C.: Observations of HONO and its precursors between urban and its surrounding agricultural fields: The vertical transports, sources and contribution to OH, Sci Total Environ, 915, 169159, https://doi.org/10.1016/j.scitotenv.2023.169159, 2024a.

Xing, C., Liu, C., Ye, C., Xue, J., Wu, H., Ji, X., Ou, J., and Hu, Q.:

Observations of the vertical distributions of summertime atmospheric pollutants in Nam Co: OH production and source analysis, Atmospheric Chemistry and Physics, 24, 10093–10112, https://doi.org/10.5194/acp-24-10093-2024, 2024b.

Xing, C., Wei, S., Li, Y., Jiao, P., Liu, C., Chen, J., Wang, W., Peng, H., Song, Y., and Liu, C.: Fast-hyperspectral imaging remote sensing: Emission quantification of NO2 and SO2 from marine vessels, Light Sci Appl, 14, 308, https://doi.org/10.1038/s41377-025-01922-x, 2025.

Xue, C., Ye, C., Zhang, C., Catoire, V., and Mu, Y.: Evidence for Strong HONO Emission from Fertilized Agricultural Fields and its Remarkable Impact on Regional O 3 Pollution in the Summer North China Plain, ACS Earth and Space Chemistry, 5, https://doi.org/10.1021/acsearthspacechem.0c00314, 2021.

Xue, C., Ye, C., Kleffmann, J., Zhang, C., Catoire, V., Bao, F., Mellouki, A., Xue, L., Chen, J., Lu, K., Zhao, Y., Liu, H., Guo, Z., and Mu, Y.: Atmospheric measurements at Mt. Tai – Part I: HONO formation and its role in the oxidizing capacity of the upper boundary layer, Atmospheric Chemistry and Physics, 22, 3149–3167, https://doi.org/10.5194/acp-22-3149-2022, 2022.

Xue, L., Zhu, Y., Gao, J., Zhong, X., Cui, C., Wang, S., Jiang, Z., Sun, Y., Li, Q., Zhang, Y., Li, H., Zhang, Y., Wang, S., Zhao, M., Shen, H., Zhang, Y., Tang, G., Wang, T., and Wang, W.: Critical transition of urban ozone formation regime in the North China Plain, Natl Sci Rev, 13, nwaf596, https://doi.org/10.1093/nsr/nwaf596, 2026.

Yang R., Liu Z., Wang W., Zhu W., Tang G., Hu B., Cheng X., and Ma Z.: Budget analysis of high nitrous acid (HONO) events and its role on ozone formation during springtime of Beijing, qhyhjyj, https://doi.org/10.3878/j.issn.1006-9585.2025.25013, 2025.

Yang, X., Lu, K., Ma, X., Gao, Y., Tan, Z., Wang, H., Chen, X., Li, X., Huang, X., He, L., Tang, M., Zhu, B., Chen, S., Dong, H., Zeng, L., and Zhang, Y.: Radical chemistry in the Pearl River Delta: observations and modeling of OH and HO_2 radicals in Shenzhen in 2018, Atmospheric Chemistry and Physics, 22, 12525–12542, https://doi.org/10.5194/acp-22-12525-2022, 2022.

Ye, C., Lu, K., Ma, X., Qiu, W., Li, S., Yang, X., Xue, C., Zhai, T., Liu, Y., Li, X., Li, Y., Wang, H., Tan, Z., Chen, X., Dong, H., Zeng, L., Hu, M., and Zhang, Y.: HONO chemistry at a suburban site during the EXPLORE-YRD campaign in 2018: formation mechanisms and impacts on O_3 production, Atmospheric Chemistry and Physics, 23, 15455–15472, https://doi.org/10.5194/acp-23-15455-2023, 2023.

Zhang, J., Lian, C., Wang, W., Ge, M., Guo, Y., Ran, H., Zhang, Y., Zheng, F., Fan, X., Yan, C., Daellenbach, K. R., Liu, Y., Kulmala, M., and An, J.: Amplified role of potential HONO sources in O_3 formation in North China Plain during autumn haze aggravating processes, Atmospheric Chemistry and Physics, 22, 3275–3302, https://doi.org/10.5194/acp-22-3275-2022, 2022.

Zhang, W., Tong, S., Jia, C., Wang, L., Liu, B., Tang, G., Ji, D., Hu, B., Liu, Z., Li, W., Wang, Z., Liu, Y., Wang, Y., and Ge, M.: Different HONO Sources for Three Layers at the Urban Area of Beijing, Environ. Sci. Technol., 54, 12870–12880, https://doi.org/10.1021/acs.est.0c02146, 2020.

Zong, R., Yang, X., Wen, L., Xu, C., Zhu, Y., Chen, T., Yao, L., Wang, L., Zhang, J., Yang, L., Wang, X., Shao, M., Zhu, T., Xue, L., and Wang, W.: Strong ozone production at a rural site in theNorth China Plain: Mixed effects of urban plumesand biogenic emissions, Journal of Environmental Sciences, 71, 261–270, https://doi.org/10.1016/j.jes.2018.05.003, 2018.

Zou, T., Xing, C., Xue, J., Li, Q., Tan, W., Wu, Z., and Liu, C.: Transport characteristics of urban and rural aerosols based on vertical observations and deep learning predictions, Atmospheric Research, 315, 107876, https://doi.org/10.1016/j.atmosres.2024.107876, 2025.